Key Points:
- New FPI observation for the polar upper atmospheric winds and temperature is initiated at Korean Antarctic station in 2014
- HWM14 and TIEGCM are evaluated for polar cap region by comparing FPI wind measurements
- The effects of intense geomagnetic storm on 17 March 2015 on thermospheric wind and temperature are investigated in the polar cap region

Polar Thermospheric Winds and Temperature Observed by Fabry-Perot Interferometer at Jang Bogo Station, Antarctica

Changsup Lee[1] (iD), Geonhwa Jee[1] (iD), Qian Wu[2] (iD), Ja Soon Shim[3] (iD), Damian Murphy[4] (iD), In-Sun Song[1] (iD), Hyuck-Jin Kwon[1] (iD), Jeong-Han Kim[1] (iD), and Yong Ha Kim[5] (iD)

[1]Korea Polar Research Institute, Incheon, South Korea, [2]High Altitude Observatory, NCAR, Boulder, CO, USA, [3]CUA/NASA GSFC, Greenbelt, MD, USA, [4]Australian Antarctic Division, Kingston, Tasmania, Australia, [5]Department of Astronomy, Space Science and Geology, Chungnam National University, Daejeon, South Korea

Abstract Upper atmospheric neutral winds and temperature have been observed by the Fabry-Perot interferometer (FPI) which was installed at Jang Bogo Station (JBS), Antarctica, in 2014. Since JBS is mostly located within the polar cap region, the observed thermospheric winds at 250 km show strong diurnal variations with notable antisunward motions due to the effects of plasma convection. The winds at 87 km, on the other hand, show semidiurnal variations due to the lower atmospheric tidal effects. We found that the winds from green line emission show largely diurnal variations, unlike the other independent observations, which might be due to the auroral contamination. The horizontal wind model 2014 winds at 250 km show reasonable agreement with FPI winds, while large discrepancies exist at 87 km in terms of seasonal variations. There is a distinctive asymmetric seasonal variation of the thermospheric zonal wind in the dusk and dawn sectors. FPI temperatures at 250 km show a fairly close correlation with *Kp* index, especially in 2015 when the geomagnetic activity is stronger. However, the temperatures at 87 km are mostly independent on *Kp* index. Finally, during the intense geomagnetic storm, thermospheric winds and temperature are significantly disturbed and Thermosphere Ionosphere Electrodynamics General Circulation Model simulations are in surprisingly good agreement with observation for winds but the temperatures are significantly underestimated during the whole storm period.

1. Introduction

Upper atmosphere in the polar region is significantly affected not only by atmospheric waves from the lower atmosphere but also by solar radiation and energetic particles originated from the space. An enormous amount of energy stored in the magnetosphere by interactions with solar wind enters the polar upper atmosphere. This energy leads to a large-scale plasma convection, currents, and heating in the polar ionosphere and then affects the neutral atmosphere mainly via ion-neutral interactions. Neutral winds in the region are accelerated by ion drag associated with plasma convection driven by magnetospheric electric field. In particular, during storm periods, the intense plasma convection drives neutral winds up to several hundreds of meters per second and the intensified neutral winds may keep the plasma convection for a while even after the storm has ended, which is called the flywheel effect (Deng et al., 1991). Hence, understanding the thermospheric neutral winds is of great importance for characterizing global-scale structure of the ionosphere determined by momentum, energy, and composition changes occurring throughout the upper atmosphere. During geomagnetic storm period, for example, enhanced equatorward winds from high-latitude region push plasma along the magnetic field to higher-altitude region with smaller O/N_2 ratio in the midlatitude region, which reduces recombination rate and thereby enhances the plasma density (Fuller-Rowell et al., 2008; Prölss, 1997).

Simultaneous observations of neutral wind and plasma convection in the high-latitude region are of utmost importance for probing the coupling processes in the ionosphere, thermosphere, and magnetosphere. The Super Dual Auroral Radar Network has been used to observe plasma convection in the entire high-latitude region (Ruohoniemi & Baker, 1998). For neutral wind observations, ground-based Fabry-Perot interferometers (FPIs) have been operated in the polar region, but the spatial coverage is much more limited, especially, in the Southern Hemisphere (Emmert et al., 2006; Förster et al., 2008; Killeen et al., 1995). The FPIs have been widely used to investigate mesospheric and thermospheric dynamics over the past few decades (Meriwether, 2006).
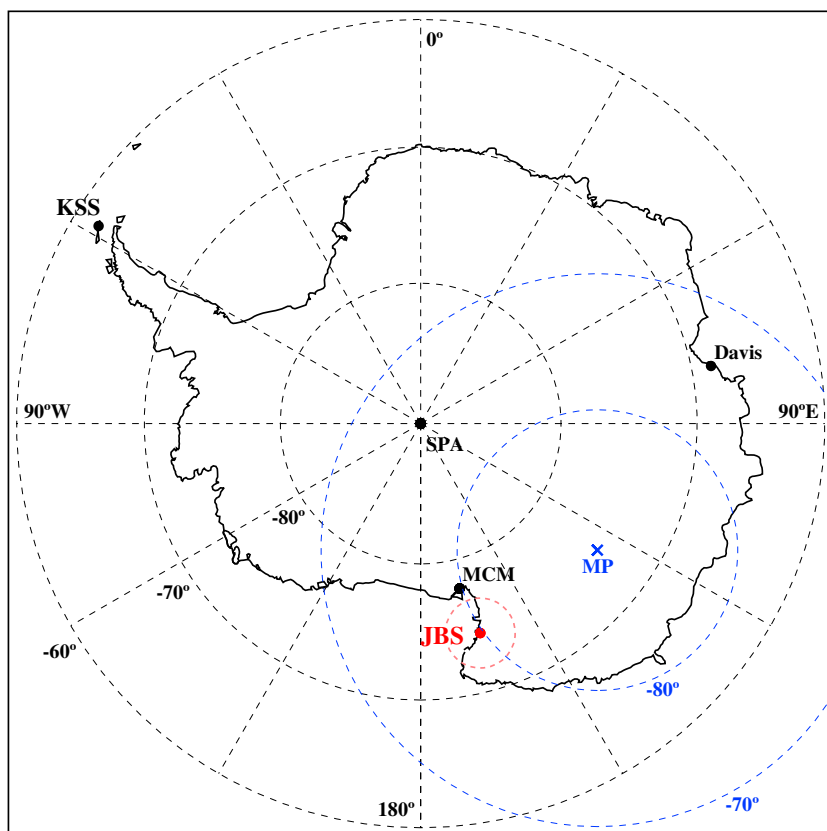
Figure 1. Location of the Jang Bogo Station (JBS). Geomagnetic latitudes are marked with blue dotted circles around geomagnetic South Pole (MP). The field of view of the JBS FPI is indicated by red dashed circle assuming the 630.0 nm emission height of 250 km.

In the northern midlatitude region, the multisite FPI network was recently deployed to investigate temporal evolution of thermospheric winds and temperatures with extended spatial coverage (Makela et al., 2012, 2014; Meriwether, 2006). In the southern polar region, only a few FPIs are currently operating and most recently Korea Polar Research Institute installed one in March 2014 at Jang Bogo Station (JBS), the second Korean Antarctic station, located in the polar cap region (Wu et al., 2017).

In this study, we present the results of the analysis of the first 2 year observations of JBS-FPI to examine polar thermospheric winds in comparison with horizontal wind model 2014 (HWM14). National Center for Atmospheric Research (NCAR) Thermosphere Ionosphere Electrodynamics General Circulation Model (TIEGCM) was also utilized to compare with the FPI observations during intense geomagnetic storm on 17 March 2015.

2. Observation and Data

2.1. Fabry-Perot Interferometer at Jang Bogo Station

The Fabry-Perot interferometer (FPI) has been widely used to study the climatology of upper atmospheric winds (Wu et al., 2008, 2017) and temperatures (Meriwether et al., 2008) and to investigate their behaviors under different conditions such as solar and geomagnetic activities. In order to observe the neutral winds and temperature in the southern polar region, the FPI was installed in March 2014 at Jang Bogo Station (JBS), the second Korean Antarctic Research base, in Terra Nova Bay, Antarctica (74.62°S 164.22°E), which is located in the polar cap region (79°S in magnetic latitude, MLAT). Figure 1 shows the location of JBS and observation coverage with red line emission in the thermosphere. The JBS FPI is developed by National Center for Atmospheric Research (NCAR). It is a high-resolution spectrometer capable of detecting small wavelength shifts with a 10 cm clear aperture etalon which is identical to the FPI at Resolute Bay, Canada (Wu et al., 2004).

The JBS FPI has been continuously observing the airglow emissions to measure neutral winds and temperatures from upper mesosphere (~87 km) up to middle thermosphere (~250 km) at clear night. The standard operating mode is performed by a dual-mirror sky scanner viewing a zenith and four directions at a zenith angle of 45° at the azimuths of 0°, 90°, 180°, and 270° to minimize unnecessary assumptions in the calculation of meridional and zonal winds. A frequency-stabilized HeNe calibration laser provides reference position and width of interference pattern. Three optical filters are used to collect nightglow emissions from three different height layers of 87 km, 97 km, and 250 km with wavelengths of OH 892.0 nm, OI-Green 557.7 nm, and OI-Red 630.0 nm, respectively. A specific optical characteristic of the JBS FPI operation is presented in Table 1. The measurements of the Doppler shift and broadening of emission line profiles are enable us to estimate neutral winds and temperatures, respectively. The FPI data processing method used in this study is identical to Wu et al. (2012). In the analysis process, wind data were excluded if the wind errors are greater than 10 ms^{-1} for lower two emissions (892.0 nm, 557.7 nm) and 25 ms^{-1} for 630.0 nm emission.

2.2. Meteor Radar at Davis Station

Meteor radar (MR) at Davis Station (68.6°S 78.0°E, MLAT 75°S) has been operated by Australian Antarctic Division since 2005 to continuously monitor neutral winds in the magnetic local time (MLT) region. The Davis MR observes meteor-ionized

Table 1
Characteristics of FPI Optical Filter and Corresponding Wind Errors

Emission (wavelength, nm)	Integration time	Wind errors	Altitude
OH (892.0)	3 min	6 m/s	87 km
O (557.7)	3 min	1 m/s	97 km
O (630.0)	5 min	2–6 m/s	250 km

trails at a frequency of 33.2 MHz with an antenna configuration of a single all-sky transmit antenna and an interferometric receiving array composed of two perpendicular baselines spaced at 2.0 and 2.5 times the radar wavelength. It provides hourly mean neutral winds in the MLT region between 80 and 100 km with a 2 km height resolution (Holdsworth et al., 2008). We used the Davis meteor wind data during 10 days of winter solstice in 2014–2015 to compare JBF FPI wind from OH and green line emissions in this study.

2.3. Aura MLS Temperature

The neutral temperature data at OH airglow emission height (~87 km) were obtained from Aura satellite observations near JBS. The Aura satellite is in a Sun-synchronous polar orbit at an altitude of 705 km with an inclination of 98.2° (Schwartz et al., 2008; Waters et al., 2006). The MLS instrument on board the Aura satellite measures thermal microwave emissions to derive the temperatures and constituent volume mixing ratios on the fixed pressure surfaces from the troposphere to the mesosphere. The MLS looks forward direction and vertically scans the Earth's atmospheric limbs in the orbital plane from the surface up to about 90 km every 24.7 s. The horizontal resolution for temperature is 165 km along the orbital track and 12 km across the track. In this study, we used the MLS data recorded at nighttime within a distance of 400 km around JBS to directly compare the satellite data with the FPI observations over the entire period.

3. Models

3.1. HWM14

The horizontal wind model (HWM) describes statistical behaviors of neutral winds from surface to about 500 km and has been continuously updated based on a wide range of observational data and theoretical consideration. The HWM14 is the latest updated model for better description of the upper thermospheric wind by including additional ground-based FPI measurements of the 630 nm airglow emission and GOCE satellite data (Drob et al., 2015). HWM14 thermospheric winds, however, still rely on a sparse collection of data from a variety of sources, and there are significant challenges to represent neutral wind in the polar MLT region where complicated energy and momentum budget exists. Therefore, it is necessary to ingest more wind measurements into the model to improve the model prediction capability.

3.2. TIEGCM

The NCAR Thermosphere Ionosphere Electrodynamics General Circulation Model (TIEGCM) is a self-consistent first-principles thermosphere ionosphere model which solves the three-dimensional momentum, energy, and continuity equations for neutral and ion species on each pressure surface (Kwak et al., 2007; Qian et al., 2014; Richmond et al., 1992; Roble et al., 1988). It provides thermospheric and ionospheric parameters such as neutral and ionospheric compositions, neutral winds and temperature, and ion/electron temperature from 97 km to ~500 km in the interval of one-half scale height. In this study, the TIEGCM (version 2.0) was run with a 2.5 × 2.5° longitude-latitude grid and 10 min temporal resolution for the great storm event in March 2015. At the lower boundary, atmospheric tides were specified using the Global Scale Wave Model (Hagan & Forbes, 2002). The Weimer ion convection model (Weimer, 2005) was adopted for the high-latitude electric potential.

4. Results and Discussions

FPI data have been collected at JBS from April 2014 to October 2015 to investigate winds and temperature in the mesosphere and thermosphere over the polar cap region. The current state-of-the-art model of the neutral wind climatology, HWM14 is used to compare with FPI wind measurements for seasonal variations. The thermospheric wind and temperature responses to the great geomagnetic storm occurred on 17 March 2015 are also examined by comparison with TIEGCM model outputs.

4.1. Neutral Winds in the Polar Upper Atmosphere
4.1.1. Local Time Variations of Neutral Winds

The upper atmospheric neutral winds observed by the JBS FPI are presented in Figure 2 from April 2014 to October 2015. Data gap was minimal over the whole observation period due to good weather conditions. The 30 day averaged wind vectors around the central date (day of year: 172) of winter solstice are also presented on the right panels of the figure at corresponding heights of 250 km, 97 km, and 87 km from top to
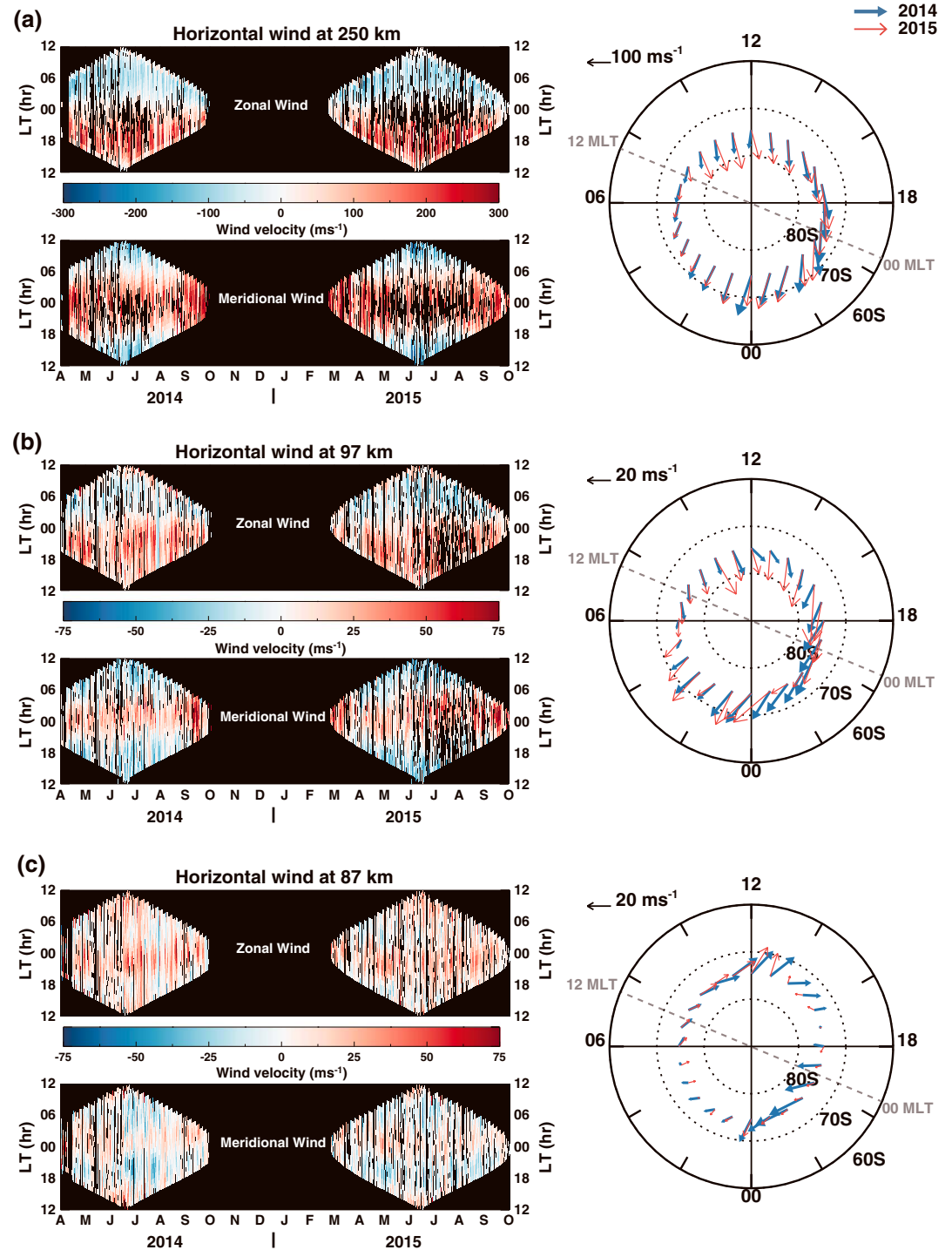
Figure 2. Neutral winds including zonal (top) and meridional (bottom) component within polar cap region obtained by FPI measurements from April 2014 to Oct 2015. FPI winds are collected from three separated airglow layers from (a) 250 km, (b) 97 km, (c) and 87 km. The variation of observational period in local time is caused by seasonal change of the length of nighttime in the southern high-latitude region. Two-dimensional wind vectors in geographic coordinates with local solar time are also presented in the right dials.

bottom. The most prominent features of the neutral winds in Figure 2 are the dominant diurnal and semidiurnal variations of the winds at 250 km and 87 km altitudes, respectively. And the local time variation at 97 km is a mixture of the two altitude regions. These features are more readily characterized in Figure 3, which presents the local time variations of the winds during nighttime period when the data
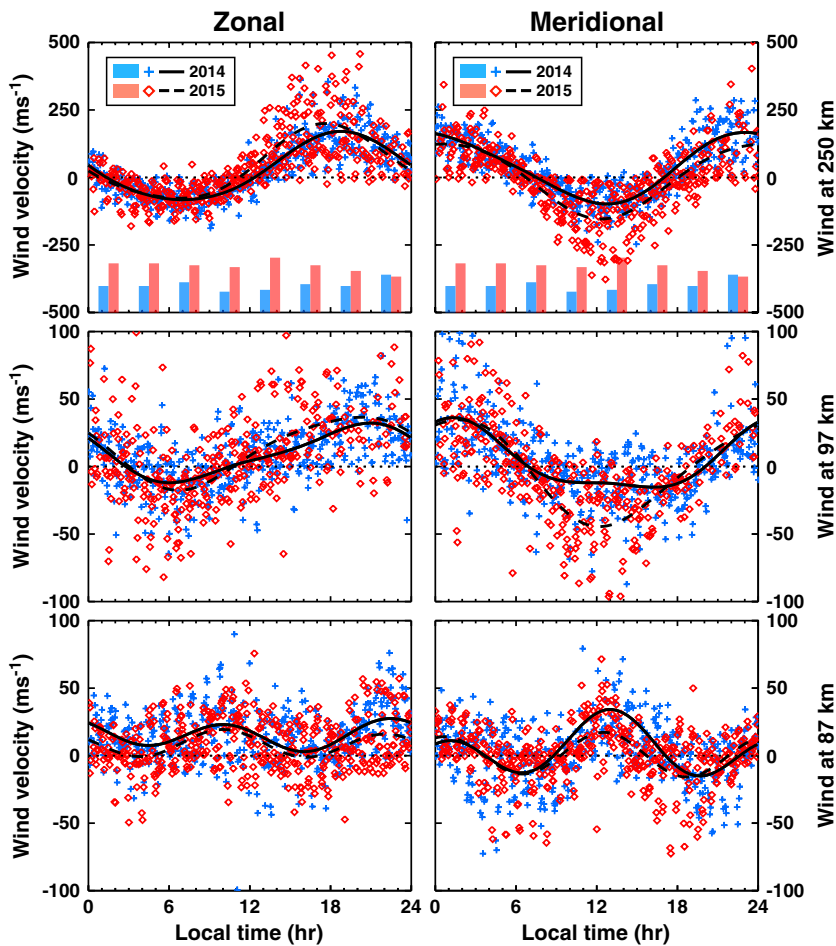
Figure 3. Local time series of (left column) zonal and (right column) meridional winds at (top row) 250 km, (middle row) 97 km, (bottom row) and 87 km observed for 10 days in the middle of winter in 2014 (blue cross)/2015 (red diamond). Least squares fit lines are presented as solid and dashed lines for the 2 years, respectively. The 10 day averaged Kp indices are depicted by blue (2014) and red (2015) boxes in Figure 3 (top row), respectively.

were collected more than 20 h d⁻¹. The least squares fitting curves with mean, diurnal, and semidiurnal variations are also shown with solid (2014) and dashed (2015) lines, respectively. The dominant antisunward wind at 250 km can be explained by strong ion drag associated with plasma convection in combination with solar-driven pressure gradient force in the polar cap region. Note that the wind scatters from the fitting cures are largely greater in 2015 than in 2014. This large scatter is probably related to the stronger geomagnetic activity in 2015 than in 2014 as depicted by color bars for mean Kp values in 2014 (blue) and 2015 (red) in Figure 3 (top row). The local time variations of the high-latitude thermospheric wind were also reported by Emmert et al. (2006).

The neutral winds from OH airglow emissions at about 87 km altitude show evident semidiurnal features which is dominant in the high-latitude MLT region. Also note that the zonal wind is mostly positive (i.e., eastward) in winter and precedes the meridional wind by about 3 h. These semidiurnal features at 87 km altitude are evidently affected from the lower atmospheric tide (Song et al., 2017; Wu et al., 2013).

At 97 km altitude, the diurnal variations of the neutral winds from green line emissions appear to be a mixture of diurnal variation in the higher-altitude region and semidiurnal variation in the lower altitude region. In the polar region, however, the neutral winds from green line emissions need a careful interpretation due to the existence of auroral emissions with an identical wavelength of 557.7 nm but at much higher altitude of about 150 km altitude (Won et al., 1999). Despite only 10 km higher than OH winds, the local time variations of green line winds are unexpectedly closer to red line winds in Figure 3. Be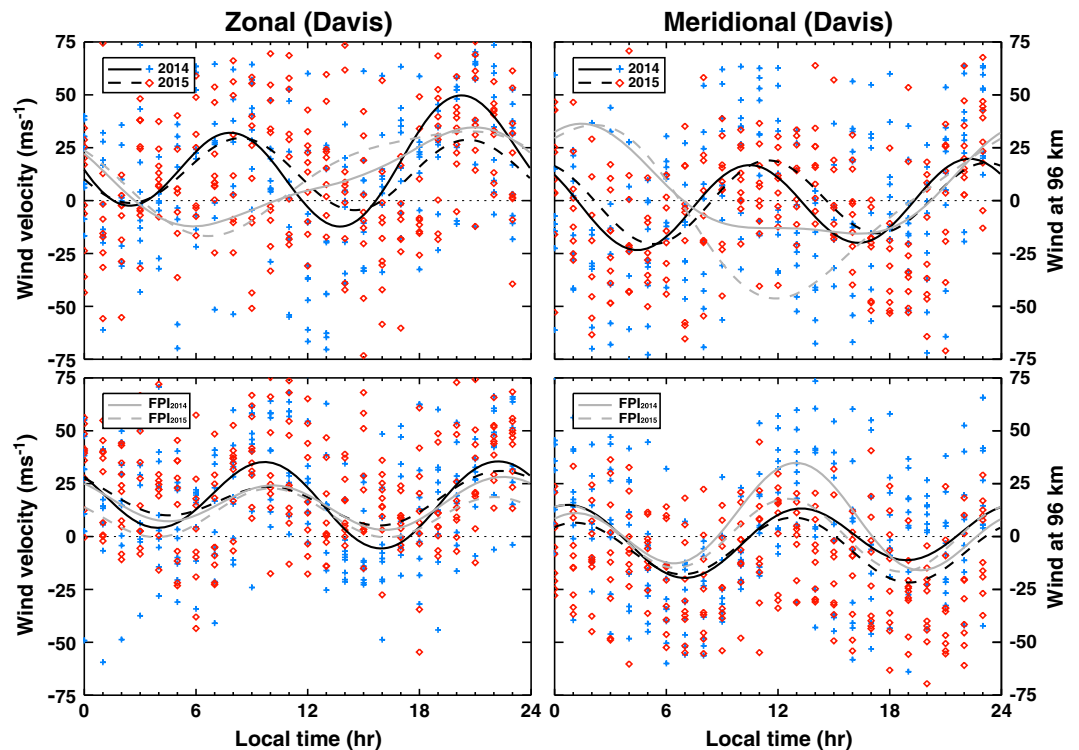cause the diurnal variation in the high-latitude MLT wind is known to be very weak (Forbes, 1982; Lee et al., 2013), large diurnal variations observed by FPI might be attributed to auroral emissions occurring at much higher altitude, being more affected by plasma convection rather than lower atmospheric semidiurnal tide. Furthermore, it is hard to believe that the effects of the ion drag originating from the plasma convection on the neutral dynamics reach down to the altitude as low as 97 km altitude (Kwak & Richmond, 2007). Meridional winds from red line at local noon show strong poleward direction, while the winds from OH at noon show strong equatorward direction in Figure 3. These two components with entirely opposite directions are well mixed in the winds from green line emission showing distorted sinusoidal shape at local noon in 2014. However, the wind in 2015 shows pronounced diurnal features and the semidiurnal effects are hardly seen. Considering higher geomagnetic activity in 2015, the effects of plasma convection on the neutral winds of the year are probably dominant over the semidiurnal tidal effects from the lower atmosphere. In order to evaluate whether the green line winds are contaminated by the auroral emission at higher altitude, it is compared with the mesopause winds observed from the meteor radar at Davis station for 10 days around the central date of winter solstice in Figure 4. Mesospheric winds derived from the Davis meteor radar have predominant semidiurnal features and 90° phase difference between zonal and meridional winds at both 96 km and 86 km altitudes. Note that there are significant differences between meteor radar winds at 96 km and FPI winds at 97 km. This discrepancy indicates that the neutral winds below about 100 km height in the polar cap region are under the strong influence of atmospheric semidiurnal tides. Therefore, it is likely that the green line winds observed by the JBS FPI having a diurnal signature might be severely contaminated by aurora emissions existing above the

Figure 4. Local time variations of neutral winds including (left column) zonal and (right column) meridional component at (top row) 96 km and (bottom row) 86 km observed by the meteor radar at Davis Station for 10 days at winter solstice in 2014 (blue cross) and 2015 (red diamond). Solid line and dashed line indicate least squares fit lines of tidal components for the 2 years, respectively. Tidal components for JBS are depicted by gray color lines for comparison.

green line airglow layer. Simultaneous observations for the aurora will be initiated at JBS in December 2017 to confirm whether the FPI observation for green line emission at 97 km is contaminated by green aurora.

There are also additional factors to consider for the green line winds such as wind shears and height variations of airglow layers. If strong wind shears exist within an airglow layer, the FPI probably underestimates true neutral wind.

4.1.2. Seasonal Variations of Neutral Winds

Figures 5a and 5b show the seasonal variations of neutral winds from FPI observation and HWM14 in 2014 and 2015, respectively. The seasonal variations of the winds are investigated in the dawn and dusk sectors for zonal component and in the midnight sector for meridional component when the winds become maximum. There are notable asymmetric patterns in zonal wind at 250 km between the dawn and dusk sectors in both FPI observation and HWM14; in other words, the seasonal variations of dawn and dust winds show exactly the opposite phase. This asymmetry in zonal wind is probably related to the different actions of the Coriolis force and Earth's curvature, which are another main force terms in addition to pressure gradient force and ion drag to characterize the zonal wind in the polar region (Forbes, 2007; Fuller-Rowell, 1995). The meridional wind at local midnight blows toward the equator for all seasons, but the magnitude shows sufficiently large seasonal variation being maximum in summer and minimum in winter, which is in relatively good agreement between the model and observations.

In the measurements of FPI winds for all heights, large day-to-day variabilities exist and they seem to be larger in 2015 when the geomagnetic activity is stronger than in 2014. This aspect of the variabilities is also evident in the HWM14 wind at 250 km. Although the HWM14 wind predictions generally overestimate thermospheric winds at 250 km, they are in reasonable agreement with FPI observations in both magnitude and direction. At 87 km altitude, on the other hand, there are large discrepancies between observations and model, especially in the midnight meridional wind. The zonal winds also show large differences in the dawn sector, while the dusk winds are relatively in a good agreement between the observation and the model.
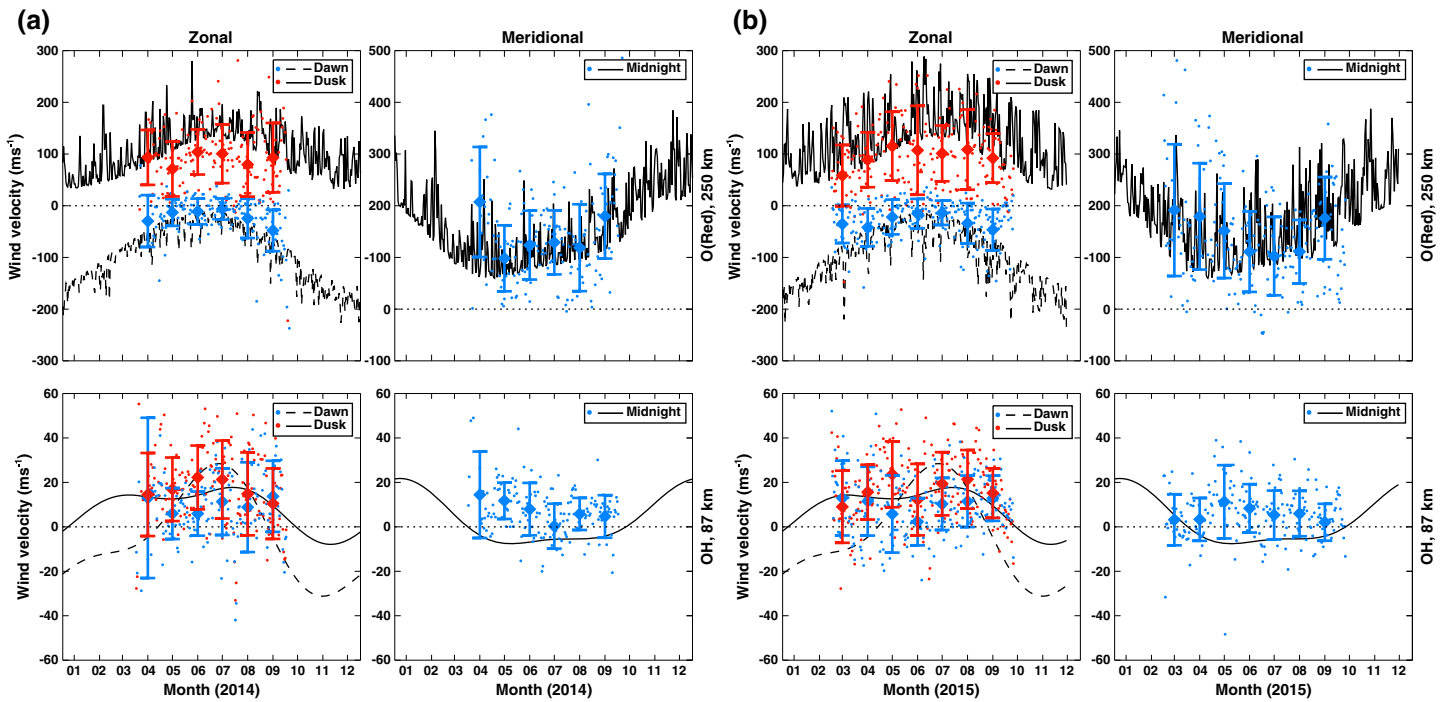
Figure 5. Seasonal variations of neutral winds from JBS FPI and HWM14 are presented daily mean values in (a) 2014 and (b) 2015. Dawnside zonal wind is presented by a blue dot (dashed line for HWM) and duskside zonal wind by a red dot (solid line for HWM). Meridional wind is presented only for midnight sector by a blue dot for FPI and a solid line for HWM. Filled diamond with error bars presents monthly mean values of corresponding wind components.

4.2. Neutral Temperatures in the Polar Upper Atmosphere

Daily mean temperatures measured by the JBS FPI at 250 km and 87 km heights are shown in Figure 6. Daily Kp indices (i.e., total Kp value for a day) are also presented at the top of the figure to show the geomagnetic activity during the observation period. There is fairly close correlation between the 250 km
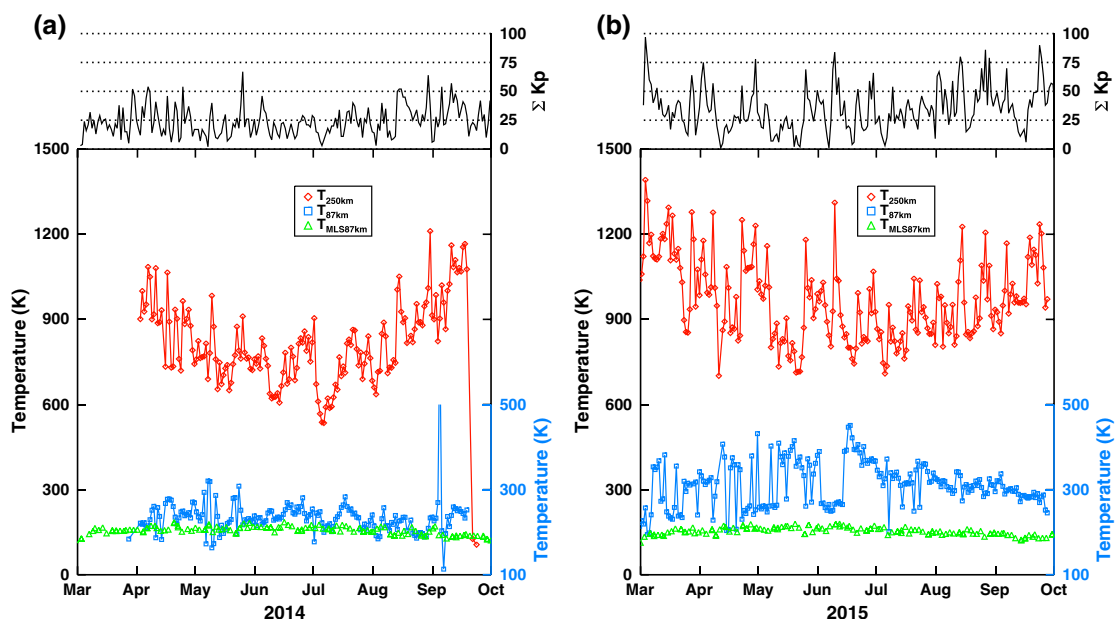

Figure 6. Daily mean FPI temperatures at 250 km (red diamond) and 87 km (blue square) in (a) 2014 and (b) 2015. Green triangle indicates MLS temperature at 87 km. Daily sum values of Kp indices are also presented on the top to show geomagnetic activity at each day.
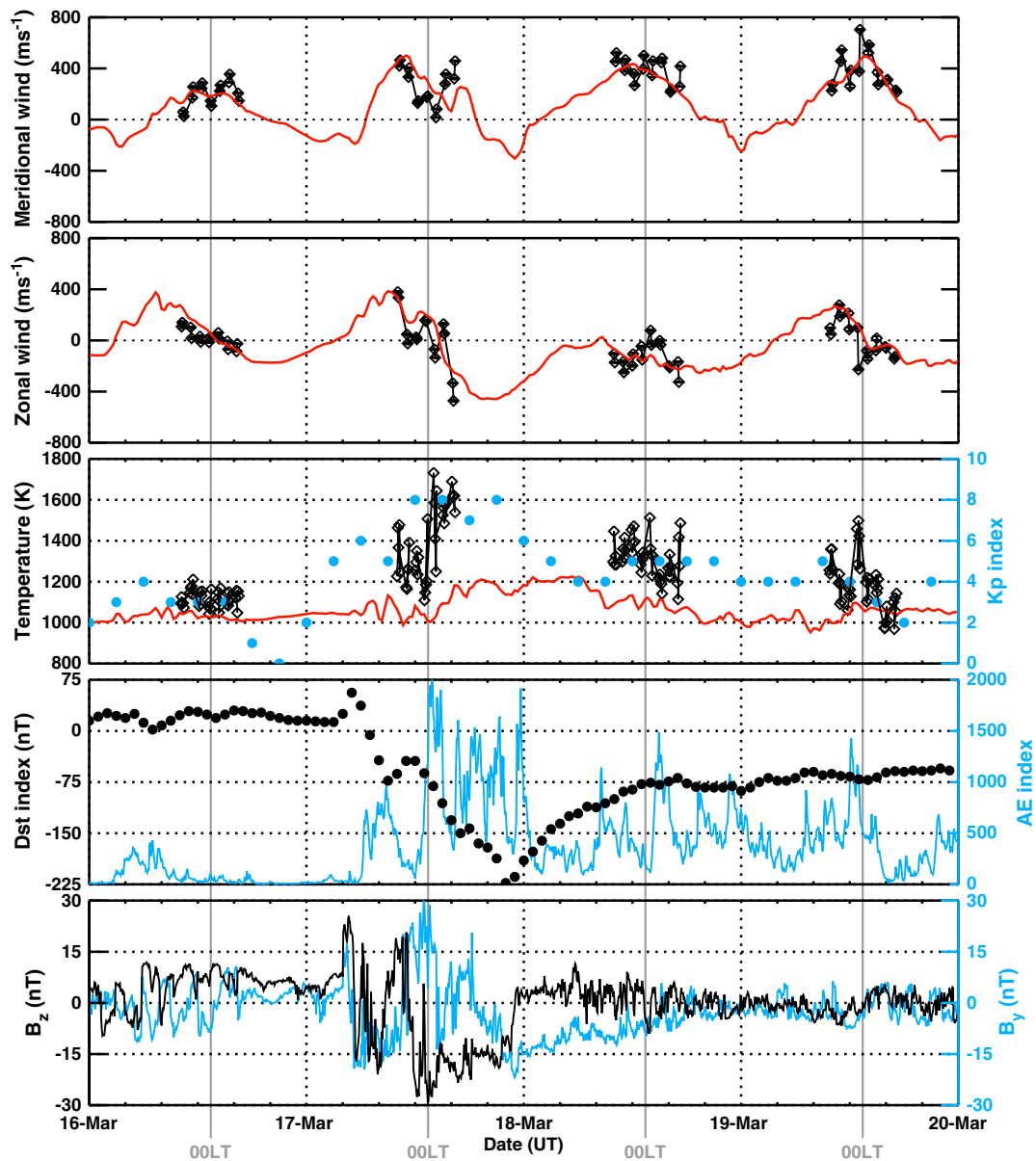
Figure 7. Thermospheric winds and temperature at 250 km during the great storm event on 17 March 2015. The open diamond illustrates the FPI observation (wind/temperature), and blue solid line is the simulated wind and temperature from the TIEGCM. *Dst, AE* index, and IMF components are also presented for space environmental condition during the storm.

temperature and daily *Kp* variations, in particular, when the magnetic activity is stronger in 2015. Temperature at 250 km has a clear annual variation with minima in winter, and its maxima should be expected in summer. On the other hand, the temperature at 87 km seems to be completely independent of *Kp*, which may imply that thermal structure below the mesopause region is mainly determined by neutral dynamic processes such as atmospheric waves rather than Joule heating or auroral heating. For the initial validation of OH temperatures, they are compared with Aura-MLS nighttime temperature measurements. In general, the OH temperatures are slightly larger than the MLS temperatures with significant fluctuations in 2014. The OH temperatures in 2015, however, are much higher than MLS temperature, and the day-to-day fluctuations are also very large. Temperature derived from FPI observations is sensitively determined by the width of spectrum of the observed emission lines, and this unrealistically high temperature in 2015 could be caused by instrument problem that the 2-D interferogram obtained from OH airglow emission was out of focus during that period.

4.3. Thermospheric Response to Great Storm on 17 March 2015

The great G4-scale geomagnetic storm ($Kp_{max} = 8$) of solar cycle 24 was commenced at 14 UT on 17 March 2015 and sustained G3/G4 levels for 12 h. Although the FPI observation was limited to only about 8 h d^{-1} in March, the storm time responses to the neutral winds are examined by comparison with TIEGCM. During 4 days around the storm, the winds and temperature from FPI were displayed with TIEGCM outputs in Figure 7. The geomagnetic indices including Kp, Dst, AE, and interplanetary magnetic field (IMF) B_z and B_y components are also presented during the storm time period. FPI winds at around midnight at JBS within polar cap region blow equatorward in meridional direction and shift from east to west in zonal direction for prestorm period. When the storm breaks out, all the magnetic indices increase dramatically and IMF B_z quickly moves southward and IMF B_y is also strongly disturbed. During the main phase of the storm, FPI winds and temperature almost instantly respond to the storm; there are severe changes of wind and significant temperature enhancement. TIEGCM wind prediction is fairly consistent with FPI observations, but the temperature prediction is very different from the observations. The zonal wind direction changes from east to west at midnight, which is also predicted by TIEGCM. The meridional wind abruptly changes from northward of ~400 ms^{-1} to a few tens of ms^{-1} within 3 h and then back to northward up to 400 ms^{-1}. This bite-out structure in the meridional wind near midnight is associated with a significant distortion of the ionospheric plasma convection from the antisunward motion due to the large fluctuations of IMF B_z during the main phase of the storm. This dependence of the polar thermospheric wind on the direction of the IMF B_z component is consistent with previous study with FPI observation in the northern polar cap region (Killeen et al., 1995). It should be noted that the meridional wind continues to be enhanced over 400 ms^{-1} during the recovery phase.

The FPI temperature at 250 km increases dramatically by about 650 K during the main phase of the storm and cools down to prestorm condition as Kp index goes down to the prestorm level. This behavior of thermospheric temperature implies that the primary heating source of the thermosphere in the polar cap region is related to the enhanced ion-neutral collisions. Note that the TIEGCM temperature prediction notably underestimates the neutral temperature enhancement only by about 200 K (solid line in the third panel of Figure 7). Huang et al. (2016) also reported that TIEGCM model predicted much lower thermospheric temperature changes compared with the FPI temperature measurements at Resolute Bay during two moderate magnetic storms in January 2005. This implies that the magnetospheric energy inputs responsible for neutral heating in the model should be improved in the polar cap region.

5. Summary

The neutral winds and temperature in the polar upper atmosphere have been observed by the FPI at Korean second Antarctic base, Jang Bogo Station (JBS), since 2014. JBS is located in the polar cap (79°S in magnetic latitude) and allows us to observe the neutral winds and temperature variations generated by the ion-neutral interactions. The observed FPI data for 2 year period of 2014–2015 were analyzed to study on the characteristics of the mesospheric and thermospheric winds and temperature within the geomagnetic polar cap region. The neutral winds at 250 km consistently blow in the antisunward direction with distinctive diurnal variations associated with plasma convection. The mesospheric wind at 87 km, on the other hand, shows clear semidiurnal signature, primarily originated from the lower atmospheric semidiurnal tides. Unlike the other independent observations, the FPI winds at 97 km altitude are mostly diurnal with a hint of semidiurnal component, which might be severely affected by green line auroral emissions occurring at much higher altitude above the green line airglow emission layer. Simultaneous observations for the aurora are required to confirm whether the FPI observations are contaminated from the auroral emission.

The HWM14 winds at 250 km show reasonable agreement with FPI wind observations in both zonal and meridional components, while large discrepancies exist at 87 km winds in terms of seasonal variations. There is a distinctive asymmetric seasonal variation of the thermospheric zonal wind in the dusk and dawn sectors. Both the model and observation for the thermospheric winds at 250 km show larger day-to-day variabilities in 2015 than in 2014, probably due to the stronger geomagnetic activity in 2015.

FPI temperatures at 250 km show a good correlation with daily sum of Kp index. In particular, when the geomagnetic activity is stronger in 2015, the day-to-day variations of temperature are highly correlated with Kp index. However, the temperatures at 87 km are mostly independent on Kp index. The FPI temperatures at 87 km are generally higher than MLS measurements.

During the intense geomagnetic storm on 17 March 2015, it is observed that thermospheric winds and temperature are significantly disturbed. The TIEGCM simulations are in surprisingly good agreement with observation for winds, but the temperatures are significantly underestimated during the whole storm period.

References

Deng, W., Killeen, T. L., Burns, A. G., & Roble, R. G. (1991). The flywheel effect: Ionospheric currents after a geomagnetic storm. *Geophysical Research Letters*, *18*, 1845–1849. https://doi.org/10.1029/91GL02081

Drob, D. P., et al. (2015). An update to the horizontal wind model (HWM): The quiet time thermosphere. *Earth and Space Science*, *2*, 301–319. https://doi.org/10.1002/2014EA000089

Emmert, J. T., Faivre, M. L., Hernandez, G., Jarvis, M. J., Meriwether, J. W., Niciejewski, R. J., … Tepley, C. A. (2006). Climatologies of nighttime upper thermospheric winds measured by ground-based Fabry-Perot interferometers during geomagnetically quiet conditions: 1. Local time, latitudinal, seasonal, and solar cycle dependence. *Journal of Geophysical Research: Space Physics*, *111*. A12302. https://doi.org/10.1029/2006JA011948

Forbes, J. M. (1982). Atmospheric tide: 2. The solar and lunar semidiurnal components. *Journal of Geophysical Research: Space Physics*, *87*(A7), 5241–5252. https://doi.org/10.1029/JA087iA07p05241

Forbes, J. M. (2007). Dynamics of the thermosphere. *Journal of the Meteorological Society of Japan*, *85B*, 193–213.

Förster, M., Rentz, S., Köhler, W., Liu, H., & Haaland, S. E. (2008). IMF dependence of high-latitude thermospheric wind pattern derived from CHAMP cross-track measurements. *Annales de Geophysique*, *26*, 1581–1595.

Fuller-Rowell, T. J. (1995). The dynamics of the lower thermosphere. *Geophysical Monograph Series*, *87*, 23–36.

Fuller-Rowell, T. J., Richmond, A. D., & Maruyama, N. (2008). Global modeling of storm-time thermospheric dynamics and electrodynamics. In P. M. Kintner, et al. (Eds.), *Midlatitude Ionospheric Dynamics and Disturbances* (Vol. 181, pp. 187–200). Washington, D. C: American Geophysical Union. https://doi.org/10.1029/181GM18

Hagan, M. E., & Forbes, J. M. (2002), Migrating and nonmigrating diurnal tides in the middle and upper atmosphere excited by tropospheric latent heat release, *Journal of Geophysical Research: Atmospheres*, *107*(D24), 4754. https://doi.org/10.1029/2001JD001236

Holdsworth, D. A., Murphy, D. J., Reid, I. M., & Morris, R. J. (2008). Antarctic meteor observations using the Davis MST and meteor radars. *Advances in Space Research*, *42*, 143–154. https://doi.org/10.1016/j.asr.2007.02.037

Huang, Y., Wu, Q., Huang, C. Y., & Su, Y.-J. (2016). Thermosphere variation at different altitudes over the northern polar cap during magnetic storms. *Journal of Atmospheric and Solar-Terrestrial Physics*, *146*(C), 140–148. https://doi.org/10.1016/j.jastp.2016.06.003

Killeen, T. L., Won, Y.-I., Niciejewski, R. J., & Burns, A. G. (1995). Upper thermosphere winds and temperatures in the geomagnetic polar cap: Solar cycle, geomagnetic activity, and interplanetary magnetic field dependencies. *Journal of Geophysical Research: Space Physics*, *100*, 21,327–21,342. https://doi.org/10.1029/95JA01208

Kwak, Y.-S., & Richmond, A. D. (2007). An analysis of the momentum forcing in the high-latitude lower thermosphere. *Journal of Geophysical Research: Space Physics*, *112*. A01306. https://doi.org/10.1029/2006JA011910

Kwak, Y.-S., Richmond, A. D., & Roble, R. G. (2007). Dependence of the high-latitude lower thermospheric momentum forcing on the interplanetary magnetic field. *Journal of Geophysical Research: Space Physics*, *112*. A06316. https://doi.org/10.1029/2006JA012208

Lee, C., Kim, Y. H., Kim, J.-H., Jee, G., Won, Y.-I., & Wu, D. L. (2013). Seasonal variation of wave activities near the mesopause region observed at King Sejong Station (62.22°S, 58.78°W), Antarctica. *Journal of Atmospheric and Solar-Terrestrial Physics*, *105–106*, 30–38. https://doi.org/10.1016/j.jastp.2013.07.006

Makela, J. J., Meriwether, J. W., Ridley, A. J., Ciocca, M., & Castellez, M. W. (2012). Large-scale measurements of thermospheric dynamics with a multisite Fabry-Perot interferometer network: Overview of plans and results from midlatitude measurements. *International Journal Geophysics*, *2012*, 1–10. https://doi.org/10.1155/2012/872140

Makela, J. J., Harding, B. J., Meriwether, J. W., Mesquita, R., Sanders, S., Ridley, A. J., … Martinis, C. R. (2014). Storm time response of the thermosphere: Observations from a network of Fabry-Perot interferometers. *Journal of Geophysical Research: Space Physics*, *119*, 6758–6773. https://doi.org/10.1002/2014JA019832

Meriwether, J. W. (2006). Studies of thermospheric dynamics with a Fabry-Perot interferometer network: A review. *Journal of Atmospheric and Solar-Terrestrial Physics*, *68*, 1576–1589. https://doi.org/10.1016/j.jastp.2005.11.014

Meriwether, J., Faivre, M., Fesen, C., Sherwood, P., & Veliz, O. (2008). New results on equatorial thermospheric winds and the midnight temperature maximum. *Annales de Geophysique*, *26*(3), 447–466. https://doi.org/10.5194/angeo-26-447-2008

Prölss, G. W. (1997). Magnetic storm associated perturbations of the upper atmosphere. In B. T. Tsurutani, et al. (Eds.), *Magnetic Storms* (Vol. 98, pp. 227–241). Washington, D. C: American Geophysical Union. https://doi.org/10.1029/GM098p0227

Qian, L., Burns, A. G., Emery, B. A., Foster, B., Lu, G., Maute, A., … Wang, W. (2014). The NCAR TIE-GCM. In J. Huba, R. Schunk, & G. Khazanov (Eds.), *Modeling the Ionosphere-Thermosphere System* (Vol. 201, pp. 73–83). Chichester, UK: John Wiley & Sons, Ltd. https://doi.org/10.1002/9781118704417.ch7

Richmond, A. D., Ridley, E. C., & Roble, R. G. (1992). A Thermosphere/Ionosphere General Circulation Model with coupled electrodynamics. *Geophysical Research Letters*, *19*(6), 601–604. https://doi.org/10.1029/92GL00401

Roble, R. G., Ridley, E. C., Richmond, A. D., & Dickinson, R. E. (1988). A Coupled Thermosphere Ionosphere General Circulation Model. *Geophysical Research Letters*, *15*(12), 1325–1328. https://doi.org/10.1029/GL015i012p01325

Ruohoniemi, J. M., & Baker, K. B. (1998). Large-scale imaging of high-latitude convection with Super Dual Auroral Radar Network HF radar observations. *Journal of Geophysical Research: Space Physics*, *103*(A), 20,797–20,811. https://doi.org/10.1029/98JA01288

Schwartz, M. J., et al. (2008). Validation of the Aura Microwave Limb Sounder temperature and geopotential height measurements. *Journal of Geophysical Research: Atmospheres*, *113*. D15S11. https://doi.org/10.1029/2007JD008783

Song, I.-S., Lee, C., Kim, J.-H., Jee, G., Kim, Y.-H., Choi, H.-J., Chun, H.-Y., & Kim, Y. H. (2017). Meteor radar observations of vertically propagating low-frequency inertia-gravity waves near the southern polar mesopause region. *Journal of Geophysical Research: Space Physics*, *122*, 4777–4800. https://doi.org/10.1002/2016JA022978

Waters, J. W., et al. (2006). The Earth Observing System Microwave Limb Sounder (EOS MLS) on the Aura satellite. *IEEE Transactions on Geoscience and Remote Sensing*, *44*, 1075–1092.

Weimer, D. R. (2005). Improved ionospheric electrodynamic models and application to calculating Joule heating rates. *Journal of Geophysical Research: Space Physics*, *110*. A05306. https://doi.org/10.1029/2004JA010884

Won, Y. I., Niciejewski, R. J., Killeen, T. L., Johnson, R. M., & Lee, B. Y. (1999). Observations of high-latitude lower thermospheric winds from Thule Air Base and Sondre Stromfjord, Greenland. *Journal of Geophysical Research: Space Physics*, *104*(A1), 25–32. https://doi.org/10.1029/1998JA900059

Wu, Q., Chen, Z., Mitchell, N., Fritts, D., & Iimura, H. (2013). Mesospheric wind disturbances due to gravity waves near the Antarctica Peninsula. *Journal of Geophysical Research: Atmospheres*, *118*, 7765–7772. https://doi.org/10.1002/jgrd.50577

Wu, Q., Gablehouse, R. D., Solomon, S. C., Killeen, T. L., & She, C.-Y. (2004). A new NCAR Fabry-Perot interferometer for upper atmospheric research. *Proceedings of SPIE*, *5660*, 218–227.

Wu, Q., Jee, G., Lee, C., Kim, J.-H., Kim, Y. H., Ward, W., & Varney, R. H. (2017). First simultaneous multistation observations of the polar cap thermospheric winds. *Journal of Geophysical Research: Space Physics*, *122*, 907–915. https://doi.org/10.1002/2016JA023560

Wu, Q., McEwen, D., Guo, W., Niciejewski, R. J., Roble, R. G., & Won, Y. I. (2008). Long-term thermospheric neutral wind observations over the northern polar cap. *Journal of Atmospheric and Solar-Terrestrial Physics*, *70*(16), 2014–2030. https://doi.org/10.1016/j.jastp.2008.09.004

Wu, Q., Wang, W., Roble, R. G., Häggström, I., & Strømme, A. (2012). First daytime thermospheric wind observation from a balloon-borne Fabry-Perot interferometer over Kiruna (68N). *Geophysical Research Letters*, *39*. L14104. https://doi.org/10.1029/2012GL052533